OPEN ACCESS



Probing the Structure and Evolution of BASS Active Galactic Nuclei through Eddington Ratios

```
Tonima Tasnim Ananna<sup>1</sup>, C. Megan Urry<sup>2</sup>, Claudio Ricci<sup>3,4</sup>, Priyamvada Natarajan<sup>5,6,7</sup>, Ryan C. Hickox<sup>1</sup>, Benny Trakhtenbrot<sup>8</sup>, Ezequiel Treister<sup>9</sup>, Anna K. Weigel<sup>10</sup>, Yoshihiro Ueda<sup>11</sup>, Michael J. Koss<sup>12,13</sup>, F. E. Bauer<sup>9,14,15</sup>, Matthew J. Temple<sup>3</sup>, Mislav Baloković<sup>2,5</sup>, Richard Mushotzky<sup>16</sup>, Connor Auge<sup>17</sup>,
  David B. Sanders<sup>17</sup>, Darshan Kakkad<sup>18</sup>, Lia F. Sartori<sup>19</sup>, Stefano Marchesi<sup>20,21</sup>, Fiona Harrison<sup>22</sup>, Daniel Stern<sup>23</sup>,
   Kyuseok Oh<sup>11,24</sup>, Turgay Caglar<sup>25</sup>, Meredith C. Powell<sup>26</sup>, Stephanie A. Podjed<sup>1</sup>, and Julian E. Mejía-Restrepo<sup>27</sup>
                              Department of Physics and Astronomy, Dartmouth College, 6127 Wilder Laboratory, Hanover, NH 03755, USA
              <sup>2</sup> Department of Physics and Yale Center for Astronomy & Astrophysics, Yale University, P.O. Box 208120, New Haven, CT 06520, USA
                      Núcleo de Astronomía de la Facultad de Ingeniería, Universidad Diego Portales, Av. Ejército Libertador 441, Santiago 22, Chile <sup>4</sup> Kavli Institute for Astronomy and Astrophysics, Peking University, Beijing 100871, People's Republic of China
                                           Department of Astronomy, Yale University, 52 Hillhouse Avenue, New Haven, CT 06520, USA
                                               Department of Physics, Yale University, P.O. Box 208121, New Haven, CT 06520, USA
                                             <sup>7</sup> Black Hole Initiative, Harvard University, 20 Garden Street, Cambridge MA 02138, USA
                                                     <sup>8</sup> School of Physics and Astronomy, Tel Aviv University, Tel Aviv 69978, Israel
9 Instituto de Astrofísica, Facultad de Física, Pontificia Universidad Católica de Chile, Campus San Joaquín, Av. Vicuña Mackenna 4860, Macul Santiago, 7820436,
                                                             <sup>10</sup> Modulos AG, Technoparkstrasse 1, CH-8005 Zurich, Switzerland
                                 <sup>11</sup> Department of Astronomy, Kyoto University, Kitashirakawa-Oiwake-cho, Sakyo-ku, Kyoto 606-8502, Japan
                                                     Eureka Scientific, 2452 Delmer Street Suite 100, Oakland, CA 94602-3017, USA
                                              <sup>13</sup> Space Science Institute, 4750 Walnut Street, Suite 205, Boulder, Colorado 80301, USA
  <sup>14</sup> Centro de Astroingeniería, Facultad de Física, Pontificia Universidad Católica de Chile, Campus San Joaquín, Av. Vicuña Mackenna 4860, Macul Santiago,
                                                                                               7820436, Chile
                               <sup>15</sup> Millennium Institute of Astrophysics, Nuncio Monseñor Sótero Sanz 100, Of 104, Providencia, Santiago, Chile
                                                  <sup>6</sup> Department of Astronomy, University of Maryland, College Park, MD 20742, USA
                                       17 Institute for Astronomy, University of Hawai'i, 2680 Woodlawn Drive, Honolulu, HI 96822, USA
                                                 Space Telescope Science Institute, 3700 San Martin Drive, Baltimore, 21218 MD, USA
                          <sup>19</sup> ETH Zurich, Institute for Particle Physics and Astrophysics, Wolfgang-Pauli-Strasse 27, CH-8093 Zurich, Switzerland
                          <sup>20</sup> INAF—Osservatorio di Astrofisica e Scienza dello Spazio di Bologna, Via Piero Gobetti, 93/3, 40129, Bologna, Italy <sup>21</sup> Provincio di Astrofisica e Scienza dello Spazio di Bologna, Via Piero Gobetti, 93/3, 40129, Bologna, Italy <sup>21</sup> Provincio della Companya Clampon University Kinard Lab of Physics Clemson SC 29634, USA
                                  Department of Physics and Astronomy, Clemson University, Kinard Lab of Physics, Clemson, SC 29634, USA
                               Department of Friysics and Astronomy, Clemson Chiversity, Island Later Hayler, Pasadena, CA 91125, USA

22 Cahill Center for Astronomy and Astrophysics, California Institute of Technology, Pasadena, CA 91125, USA
                   <sup>23</sup> Jet Propulsion Laboratory, California Institute of Technology, 4800 Oak Grove Drive, MS 169-224, Pasadena, CA 91109, USA

<sup>24</sup> Korea Astronomy & Space Science institute, 776, Daedeokdae-ro, Yuseong-gu, Daejeon 34055, Republic Of Korea

<sup>25</sup> Laidan Observatory, PO Roy 9513, 2300 P.A. Leiden, The Netherlands
                                                            Leiden Observatory, PO Box 9513, 2300 RA, Leiden, The Netherlands
                       <sup>26</sup> Kavli Institute of Particle Astrophysics and Cosmology, Stanford University, 452 Lomita Mall, Stanford, CA 94305, USA
                                                               European Southern Observatory, Casilla 19001, Santiago 19, Chile
                                   Received 2022 August 26; revised 2022 October 9; accepted 2022 October 10; published 2022 October 28
```

Abstract

We constrain the intrinsic Eddington ratio (λ_{Edd}) distribution function for local active galactic nuclei (AGN) in bins of low and high obscuration [$\log(N_{\rm H}/{\rm cm}^{-2}) \le 22$ and $22 < \log(N_{\rm H}/{\rm cm}^{-2}) < 25$], using the Swift Burst Alert Telescope 70 month/BASS DR2 survey. We interpret the fraction of obscured AGN in terms of circumnuclear geometry and temporal evolution. Specifically, at low Eddington ratios ($\log \lambda_{\rm Edd} < -2$), obscured AGN outnumber unobscured ones by a factor of \sim 4, reflecting the covering factor of the circumnuclear material (0.8, or a torus opening angle of \sim 34°). At high Eddington ratios ($\log \lambda_{\rm Edd} > -1$), the trend is reversed, with <30% of AGN having $\log(N_{\rm H}/{\rm cm}^{-2}) > 22$, which we suggest is mainly due to the small fraction of time spent in a highly obscured state. Considering the Eddington ratio distribution function of narrow-line and broad-line AGN from our prior work, we see a qualitatively similar picture. To disentangle temporal and geometric effects at high $\lambda_{\rm Edd}$, we explore plausible clearing scenarios such that the time-weighted covering factors agree with the observed population ratio. We find that the low fraction of obscured AGN at high $\lambda_{\rm Edd}$ is primarily due to the fact that the covering factor drops very rapidly, with more than half the time spent with <10% covering factor. We also find that nearly all obscured AGN at high- $\lambda_{\rm Edd}$ exhibit some broad lines. We suggest that this is because the height of the depleted torus falls below the height of the broad-line region, making the latter visible from all lines of sight.

Unified Astronomy Thesaurus concepts: Active galactic nuclei (16); Supermassive black holes (1663); X-ray surveys (1824); Astronomy data modeling (1859); Astronomical models (86); X-ray active galactic nuclei (2035); Luminosity function (942); Accretion (14)

1. Introduction

To study active galactic nuclei (AGN) comprehensively, across multiple wavelengths, we must disentangle confounding observational selection effects, to measure the underlying physical quantities like AGN mass, luminosity, and accretion rate. For example, although unobscured AGN dominate optically selected samples of highly luminous sources (e.g., Richards et al. 2002) they end up being a minority in the census of the total population (e.g., Treister et al. 2004; Gilli et al. 2007; Treister et al. 2009; Ananna et al. 2019). Similarly, radio-selected samples are dominated by radio-loud AGN, which also constitute a very small fraction of the overall AGN population (e.g., Best et al. 2005; Stawarz 2010). To get at the underlying demographics, it is important to account for both selection biases and measurement uncertainties. In the last 15 years, high-energy X-ray telescopes such as Swift Burst Alert Telescope (BAT) INTEGRAL, and NuSTAR have provided nearly unbiased X-ray-detected samples of AGN, where biases only become significant for the most heavily obscured sources (see Ricci et al. 2015; Koss et al. 2016; Ananna et al. 2022). The Swift-BAT 70 month survey provided the most sensitive map above 10 keV (Baumgartner et al. 2013). Using optical and infrared spectroscopy, the BAT AGN spectroscopic survey (BASS) provided morphology, masses, redshifts, luminosity, and obscuring column density for 752 nonblazar AGN, including 292 type II AGN (Ricci et al. 2017a; Koss et al. 2022a, 2022b). The 98% completeness in black hole mass estimates for unbeamed AGN outside of the Galactic plane comes from broad emission lines and from velocity dispersion of stars within the host galaxy bulges (Koss et al. 2022b, 2022c; Mejia-Restrepo et al. 2022).

In Ananna et al. (2022; henceforth A22) we used a Bayesian inference methodology (described in detail in Section 3 of A22, summarized here in Section 2) to calculate the bias-corrected intrinsic black hole mass function (BHMF) and Eddington ratio distribution function (ERDF) of local AGN (i.e., $0.01 \le z \le 0.3$), divided into optical broad-line/type I and narrow-line/type II AGN categories. The bias correction accounted for both Eddington bias and the effect of obscuration on apparent source brightness (and thus, obscuration-dependent survey depth). A22 found the shape of the BHMFs of type I and type II AGN to be in agreement. However, the distributions of Eddington ratios of type I and type II AGN were significantly different, and these differences prompt an interesting interpretation with far-reaching implications for AGN unification.

The original AGN unification scheme was purely geometric: viewing angle explained the major distinctions among different types of AGN. However, AGN are variable sources, sometimes changing from one type to another (e.g., Urry & Padovani 1995; Marchese et al. 2012; Braito et al. 2014; Trakhtenbrot et al. 2019; Green et al. 2022). A luminosity-dependent interpretation referred to as the receding torus model (e.g., Lawrence 1991; Simpson 2005; Oh et al. 2015) suggested that as AGN luminosity increases, since the dust sublimation radius increases, this causes the inner edge of the obscuring torus to recede. This idea was supported by the results of Ueda et al. (2003), La Franca et al. (2005), Barger et al. (2005), Simpson (2005), and Treister et al. (2008), who found a decreasing fraction of obscured AGN with luminosity.

Analysis of the BASS sample supports an alternate interpretation, where Eddington ratio rather than luminosity is the parameter that regulates how obscuring matter is distributed around AGN. Ricci et al. (2017b) used the observed BAT sample to study fractions of obscured AGN in two luminosity bins as a function of Eddington ratio. The obscured fractions in the two bins were very similar, and decreased with increasing Eddington ratio, implying that the torus structure is more fundamentally dependent on Eddington ratio than on luminosity.

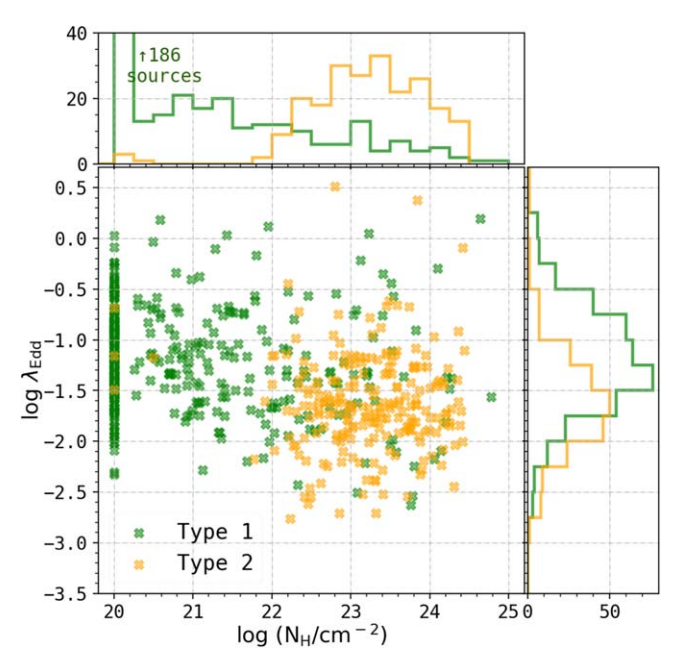


Figure 1. The distribution of type I (green crosses) and type II (orange crosses) AGN in column density-Eddington ratio space. There are 276 obscured AGN ($\log(N_{\rm H}/{\rm cm^{-2}}) \geqslant 22$), compared to 220 type II AGN (narrow lines). Similarly, there are 301 AGN with $\log(N_{\rm H}/{\rm cm^{-2}}) < 22$, and 366 type I AGN, some of which have high column densities.

This interpretation is known as the radiation-regulated unification model. The intrinsic Eddington ratio distribution function analysis for broad-line/narrow-line AGN in A22 is also in agreement with these results. Ricci et al. (2022), which is a companion paper to our analysis in this work, use the updated BASS DR2 data (Koss et al. 2022a, 2022b) to reaffirm this version of the unification scheme, and discuss evolution along the obscuration-Eddington ratio plane.

Here, we report the intrinsic space density of AGN as a function of Eddington ratio in bins of obscuration, quantified by equivalent hydrogen column density, $\log(N_{\rm H}/{\rm cm}^{-2})$. Specifically, we divide the AGN into subsamples according to the $\log(N_{\rm H}/{\rm cm}^{-2})$: $\log(N_{\rm H}/{\rm cm}^{-2}) < 22$ and $22 \le \log(N_{\rm H}/{\rm cm}^{-2}) < 25$. Intrinsic ERDFs constrained in the X-ray-based column density measurements allow us to study this AGN sample from a different perspective and compare with the ERDFs derived earlier by A22 using type I/type II (optical broad-line/narrow-line) categorization. Moreover, X-ray-based column densities provide direct insight into line-of-sight circumnuclear obscuration, and facilitate comparison with theoretical predictions. Figure 1 shows the distribution of observed type I and type II AGN in $\lambda_{\rm Edd}$ -log $N_{\rm H}$ space. The number of objects in each obscuration bin is given in Table 1.

Our Letter is structured as follows: In Section 2, we discuss the data and the analysis methodology. In Section 3, we present our results, and in Section 4 we offer a physically motivated interpretation of our results, divided into high- and low- $\lambda_{\rm Edd}$ regimes, in the context of geometric unification and transition. In Section 5, we present our conclusions. We adopt a $\Lambda{\rm CDM}$ cosmology with $h_0=0.7$, $\Omega_m=0.3$, and $\Omega_{\Lambda}=0.7$ throughout this Letter.

2. Analysis

Our main sample follows the same selection criteria as A22, and includes all unbeamed AGN over an absolute galactic latitude of 5°, and falls within $0.01 \leqslant z \leqslant 0.3$, $6.5 \leqslant \log{(M_{\rm BH}/M_{\odot})} \leqslant 10.5$

 Table 1

 Intrinsic Eddington Ratio Distribution Function in Two Obscuration Bins^a

$\log(N_{\rm H}/{\rm cm}^{-2})$ Bin	N _{obs} b	$\log \xi$	δ_1	ϵ_{λ}	$\log(\lambda_*)$
$\log(N_{\rm H}/{\rm cm}^{-2}) < 22$	301 (6)				
$\sigma = 0.3$		-4.29	$0.10^{+0.16}_{-0.00}$	$2.73^{+0.22}_{-0.16}$	$-1.064^{+0.055}_{-0.052}$
$\sigma = 0.5$		-4.26	$0.10^{+0.55}_{-0.05}$	$2.51^{+0.44}_{-0.46}$	$-1.165^{+0.112}_{-0.076}$
$22 \leqslant \log(N_{\rm H}/{\rm cm}^{-2}) \leqslant 25$	285 (4)				
$\sigma = 0.3$		-3.42	$-0.01^{+0.27}_{-0.34}$	$2.51^{+0.32}_{-0.19}$	-1.750 ± 0.093
$\sigma = 0.5$		-3.42	$0.03^{+0.30}_{-0.65}$	$2.91^{+0.38}_{-0.35}$	$-1.67^{+0.13}_{-0.14}$

Notes.

and $-3 \le \log \lambda_{Edd} \le 1$ (i.e., a total of 586 sources from the mass, redshift, and λ_{Edd} range where the BASS sample is most complete; see Figure 1 in A22). We use the masses, redshifts (Koss et al. 2022a), X-ray luminosities, and obscuration measurements (Ricci et al. 2017a) for the BASS DR2 sample to calculate Eddington ratios for these AGN.

2.1. Intrinsic Eddington Ratio Distribution Functions

While previous studies have constrained the Eddington ratio distribution function for type I/broad-line AGN (e.g., Kelly & Shen 2013; Schulze et al. 2015), A22 was the first to constrain the intrinsic Eddington ratio distribution function for obscured type II/narrow-line AGN. We briefly describe the method here (more details in Section 3.4 of A22). Using a Bayesian ensemble sampler with 50 walkers (Foreman-Mackey et al. 2013), we maximize the likelihood for the following function:

$$\ln \mathcal{L} = \sum_{i}^{N_{\text{obs}}} \ln p_i (\log M_{\text{BH},i}, \log N_{\text{H},i}, \log \lambda_{\text{E},i}, z_i), \tag{1}$$

where p_i is a convolution of the intrinsic AGN mass function and $\log \lambda_{\rm Edd}$ distribution (constrained together), comoving volume element, the area-flux curve (i.e., selection function) of the survey(s), redshift evolution function, and absorption function. As p_i is a probability distribution function, it is normalized by integrating this product over all observables:

$$p_{i, \text{ conv}}(\log M_{\text{BH}, i}, \log \lambda_{\text{E}, i}, \log N_{\text{H}, i}, z_{i}) = \frac{N_{i, \text{ conv}}}{N_{\text{tot}}}$$

$$= \frac{1}{N_{\text{tot}}} \iiint \Psi(\log M_{\text{BH}}, \log \lambda_{\text{E}}, \log N_{\text{H}}, z)$$

$$\times \Omega_{\text{sel}}(\log M_{\text{BH}}, \log \lambda_{\text{E}}, \log N_{\text{H}}, z)$$

$$\times p(\log N_{\text{H}}) p(z) \frac{dV_{C}(z)}{dz}$$

$$\times \omega(\log M_{\text{BH}, i}, \log \lambda_{\text{E}, i}, \log N_{\text{H}, i}, z_{i}|$$

$$\times \log M_{\text{BH}}, \log \lambda_{\text{Edd}}, \log N_{\text{H}}, z)$$

$$\times d \log M_{\text{BH}} d \log \lambda_{\text{Edd}} d \log N_{\text{H}} dz, \qquad (2)$$

where Ψ is the convolution of mass and Eddington ratio distribution functions. The parametric form of the intrinsic Eddington ratio distribution function is a double power law:

$$\xi(\log \lambda_{\rm Edd}) = \frac{dN}{d \log \lambda_{\rm Edd}} \propto \xi^* \times \left[\left(\frac{\lambda_{\rm Edd}}{\lambda_{\rm Edd}^*} \right)^{\delta_1} + \left(\frac{\lambda_{\rm Edd}}{\lambda_{\rm Edd}^*} \right)^{\delta_2} \right]^{-1}$$
(3)

 $\Omega_{\rm sel}$ is the selection function (area-flux curve for the BAT 70 month survey; Baumgartner et al. 2013), $p(\log N_{H,i})$ is the intrinsic absorption function for BAT AGN (from Ricci et al. 2015), $p(z_i) = 1$ as we assume negligible redshift evolution over the $0.01 \le z \le 0.3$ range, and $\frac{dV_C(z_i)}{dz}$ is the comoving volume element. The ω term allows us to convolve uncertainty in mass measurement. We assume Gaussian scatter in mass and luminosity measurements with different dispersions in A22. We report results for both $\sigma_{\rm M}=\sigma_{\lambda_{\rm Edd}}=0.3$ and 0.5 cases in Section 3, and find that the functions agree within 1σ over the range of log $\lambda_{\rm Edd}$ considered here, so only the first case is shown in the figures for clarity. The 1σ random errors on the functions are calculated using the covariance matrix, which we derive from the Markov Chain Monte Carlo chain. The formula for this error estimation is given in Appendix C of A22. Note that assuming a functional form such as a double power law leads to smaller errors than more flexible approaches for constraining space densities. We assume that the shape of the ERDF is independent of mass, because in Section 4.4 of A22, we showed that for the mass range considered for this sample $[6.5 \le \log (M_{\rm BH}/M_{\odot}) \le 10.5]$, the shape of the ERDF does not change when constrained in two mass bins independently: $[\log (M_{\rm BH}/M_{\odot}) \le 7.8 \text{ and } \log (M_{\rm BH}/M_{\odot}) \ge 8.2].$

2.2. Evolution of AGN Covering Factor at High Eddington Ratio

When the torus is stable, the ratio of obscured to overall AGN space density is equal to the population-averaged covering factor of the torus. When the radiation pressure is very high (e.g., at high $\lambda_{\rm Edd}$, the torus is unstable, and its geometry is time dependent). To disentangle the geometric and temporal aspects at high $\lambda_{\rm Edd}$ (theoretically at log $\lambda_{\rm Edd} > -1.7$; see Section 4.1), we consider two simple parametric models of how the covering factor varies over time at high $\lambda_{\rm Edd}$. We assume that after AGN are triggered from a low- $\lambda_{\rm Edd}$ phase to high $\lambda_{\rm Edd}$, they typically start with a high covering factor ($\sim 83\%$ for $\log(N_{\rm H}/{\rm cm}^{-2}) =$ 22–25 torus and \sim 60% for narrow-line-only AGN, as shown in the lower panel of Figure 2). As obscuring matter is removed because of the increased radiation pressure around an AGN, its covering factor should decrease. We consider two scenarios for the temporal dependence: (i) the rate at which the covering factor decreases is highest when there is more obscuring matter, or (ii) the covering factor initially decreases slowly due to shielding from obscuring matter, and then decreases more rapidly as more and more matter is removed. Both scenarios end with the

a Parameters defined in Equation (3).

^b Number of AGN with $\log \lambda_{\rm Edd} > 0$ in parentheses.

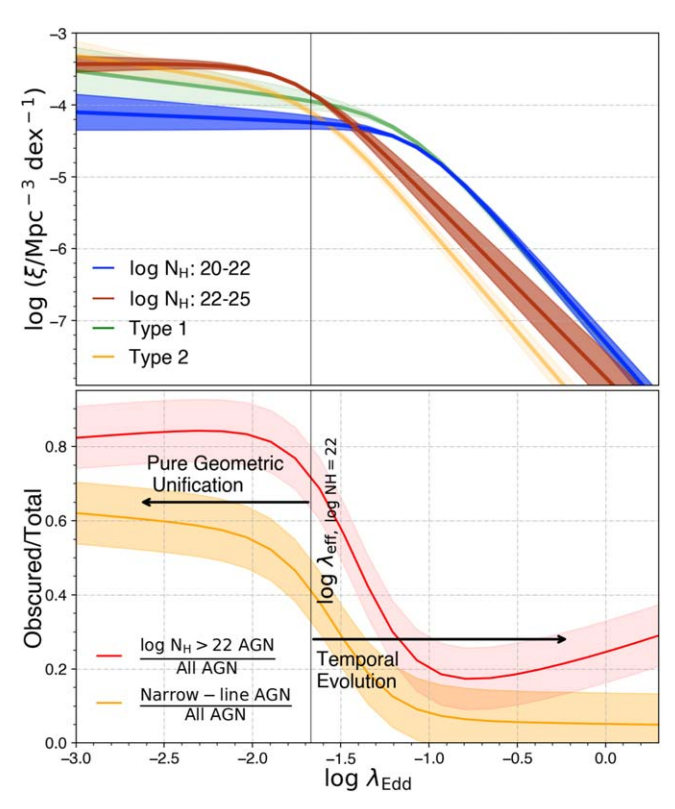


Figure 2. Top panel: Eddington ratio distribution functions for active galactic nuclei (AGN) in $\log(N_{\rm H}/{\rm cm}^{-2})=20$ –22 and $\log(N_{\rm H}/{\rm cm}^{-2})=22$ –25 bins, as well as for type I and type II AGN (from A22). Shaded regions show 1σ uncertainties. Bottom panel: ratio of obscured to overall space densities as a function of $\lambda_{\rm Edd}$. The *red line* shows ratio of $\log(N_{\rm H}/{\rm cm}^{-2})=22$ –25 AGN over all AGN, and the *orange line* shows ratio of type II AGN/all AGN. *Black vertical lines* show effective Eddington limits for $\log(N_{\rm H}/{\rm cm}^{-2}) \ge 22$ gas according to Fabian et al. (2008). At low Eddington ratios ($\lambda_{\rm Edd} < -1.7$), this ratio is high because gas is retained, while for higher Eddington ratios, gas is blown away. We suggest that at low- $\lambda_{\rm Edd}$ this ratio is equal to the pure geometric covering factor of the torus, while at high $\lambda_{\rm Edd}$, it is a time-averaged covering factor. We calculate the torus opening angle at low- $\lambda_{\rm Edd}$ and the covering factor decay rate at high $\lambda_{\rm Edd}$ using these ratios.

covering factor decreasing asymptotically such that it *may* approach zero, depending on the obscured/overall ratio. We do not force the final covering factor to equal zero at the end of the high $\lambda_{\rm Edd}$ phase as IR studies of luminous quasars show residual dust even for luminous optical quasars (e.g., Hall et al. 2004; Hopkins et al. 2004), essentially allowing the data to decide the final covering factor. We use exponential and sigmoid functions to model the behavior for scenarios (i) and (ii), respectively:

(i)
$$C_{\exp}(t) = C_0 e^{-kt}$$

(ii) $C_{\text{sigmoid}}(t) = C_0 \frac{1 + e^{-kt_0}}{1 + e^{k(t - t_0)}}$ (4)

Figure 3 shows the simulated evolution derived for a sample of 1000 AGN with the average observed covering factors (drawn from a normal distribution of $\mu=0.83$, $\sigma=0.08$ for $\log(N_{\rm H}/{\rm cm}^{-2})=22-25$ torus, and $\mu=0.6$, $\sigma=0.07$ for the narrow-line AGN). Given a set of parameters, we calculate the average covering factor for these 1000 AGN over 100 time steps. To calculate the time-averaged covering factor for these 1000 objects, we draw random times from the lifetime of each AGN, and average over the whole population. We repeat this 100 times for each set of parameters to account for the stochasticity in selecting different time steps, and choose the median. We use a Bayesian ensemble sampler to optimize these

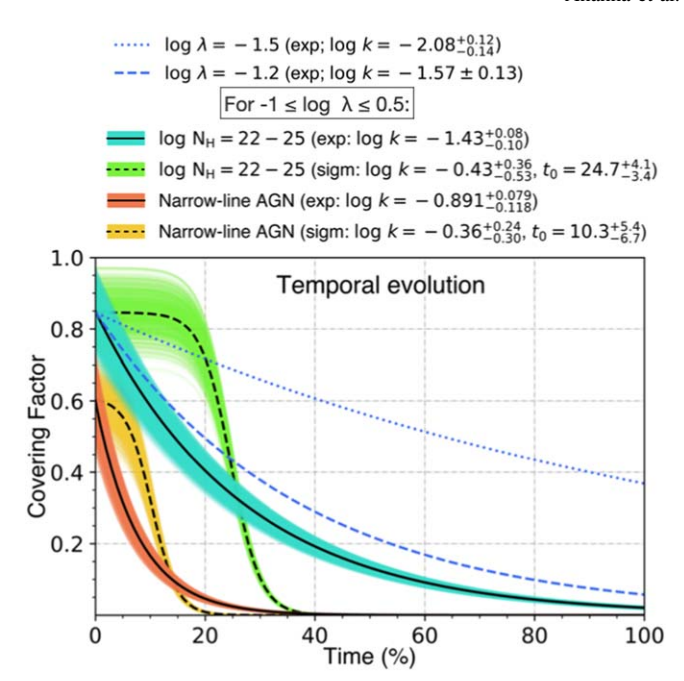


Figure 3. Decline of the covering factor after an active galactic nuclei (AGN) reaches high enough $\lambda_{\rm Edd}$ that radiation pressure exceeds the gravitational pull on obscuring matter (at $\log \lambda_{\rm Edd} \geqslant -1.7$; Fabian et al. 2008), shown for two different assumed temporal dependences (dashed and solid black lines represent sigmoid and exponential functions, respectively, as in Equation (4)), evaluated for two different definitions of obscured vs. unobscured classes (sorted by $\log N_{\rm H}$ or spectral line width). The colored lines show the decay for a 1000 AGN starting from different covering factors (see Section 2.2). Assuming that the ratio of obscured to overall AGN is a time-averaged covering factor (see bottom panel of Figure 2), we use an ensemble sampler to constrain the model parameters (shown in legend). All black lines and associated shaded regions show covering factor decay for $-1\leqslant\log\lambda_{\rm Edd}\leqslant0.5$. Exponential decay functions at two lower Eddington ratios are shown using blue lines: blue dotted lines show results for $\log\lambda_{\rm Edd}=-1.5$ and blue dashed lines show results for $\log\lambda_{\rm Edd}=-1.2$. The residual covering factor is higher at lower $\lambda_{\rm Edd}$.

functions to reproduce the obscured/overall ratio (shown in Figure 2) using a Gaussian likelihood function:

$$L(k, t_0; \text{ obs ratio}) = \frac{1}{\sqrt{2\pi\sigma_{\text{obs ratio}}^2}} \times \exp\left(-\frac{(\langle C(t)\rangle - \mu_{\text{obs ratio}})^2}{2\sigma_{\text{obs ratio}}^2}\right),$$
 (5)

where C(t) is defined in Equation (4), and only the parameter k is constrained for scenario (i).

3. Results

The intrinsic Eddington ratio distribution function in bins of $\log N_{\rm H}$ is presented in Table 1 and Figure 2. The top panel of Figure 2 shows the selection bias and measurement uncertainty-corrected Eddington ratio distributions of unabsorbed [$\log(N_{\rm H}/{\rm cm}^{-2})$: 20–22] and absorbed AGN bins [$\log(N_{\rm H}/{\rm cm}^{-2})$: 22–25], along with the type I/type II ERDFs from A22. The bottom panel shows the fraction of type II AGN and $\log(N_{\rm H}/{\rm cm}^{-2})$: 22–25 AGN as a function of $\lambda_{\rm Edd}$, calculated by dividing the ERDFs of these populations by the ERDF of all AGN.

Figure 3 shows the evolution of the geometric covering factor at high $\lambda_{\rm Edd}$ (see Equation (4)). These model parameters (k and t_0) are constrained using the ratio of obscured to the total population shown in Figure 2, at $\log \lambda_{\rm Edd} = -1.5$, -1.2, and

averaged over $-1 \le \log \lambda_{\rm Edd} \le 0.5$. The average ratios for the last bin are 0.23 ± 0.08 and $0.06 \pm +0.07$, for X-ray and optical measure of obscuration, respectively.

4. Discussion

In this work, we calculated the Eddington ratio distribution functions for obscured and unobscured AGN using X-ray measures of $N_{\rm H}$. We compare these functions to the ERDF for type I and type II AGN calculated in A22 using the same sample (all ERDFs shown in Figure 2).

At low Eddington ratio, when the circumnuclear torus is presumably stable, the ratio of the space density of obscured AGN to all AGN reflects the average covering factor of the torus. In Section 4.1, we discuss the torus at low- $\lambda_{\rm Edd}$, below the theoretical threshold where the radiation pressure exceeds the gravitational pull. At high $\lambda_{\rm Edd}$, in contrast, the gas and dust is blown away, so this ratio reflects the time-averaged covering factor. In Section 4.2, we consider the ERDF and obscured/overall ratio at higher $\lambda_{\rm Edd}$, and explore the time dependence of the covering factor using simple physically motivated models described in Section 2.2.

4.1. Low- λ_{Edd} Region: Geometric Unification

Fabian et al. (2006, 2008) pointed out that the standard Eddington ratio is calculated for fully ionized gas, whereas for partially ionized cold gas, the scattering cross-section is higher, and therefore the "effective Eddington limit" ($\lambda_{\rm eff}$) for such gas is lower. That is, colder, less ionized gas can be removed from near the AGN at lower levels of radiation pressure and thus lower Eddington limit.

In order to compare our results quantitatively with this theoretical picture, we check whether λ^* , the break in the power-law form of the Eddington ratio distribution function (see Equation (3)), corresponds to the effective Eddington ratio for dusty gas at high densities. The value of A from Figure 1 in Fabian et al. (2008) represents the ratio of scattering cross sections for dusty gas compared to ionized gas (see Equation (2) from Fabian et al. 2008), or equivalently, to $\lambda_{\rm Edd}/\lambda_{\rm eff}$. That is, the break, λ^* , should occur at $\lambda_{\rm eff}/A$ (for $\lambda_{\rm Edd}=1$). For $\log(N_{\rm H}/{\rm cm}^{-2})=22-25$, $\log\lambda^*=-1.67^{+0.13}_{-0.14}$ for $\sigma_{\log M}=\sigma_{\log\lambda}=0.5$, which is in excellent agreement with the Fabian et al. (2008) predicted value, $\log A\sim 1.67$.

Under $\lambda_{\rm eff}$ for obscured gas, both theoretically and as indicated by observations (log $\lambda_{\rm Edd} < -1.67$ according to Fabian et al. (2008) and our results, and log $\lambda_{\rm Edd} < -2$ more conservatively), the radiation pressure is too low to blow away the obscuring matter. The simple scenario that emerges from this low- $\lambda_{\rm Edd}$ region is that the pure geometric unification model (Antonucci 1993; Urry & Padovani 1995; Netzer 2015) applies in this $\lambda_{\rm Edd}$ regime, where the torus covering factor (equal to the ratio of obscured to all AGN in this regime $\lambda_{\rm Edd}$) could be as high as 83%. However, the broad-line region (BLR) is completely blocked for only 60% of the total solid angle, which could be indicative of clumpiness in the torus structure (e.g., Ramos Almeida et al. 2009; Elitzur 2012; Stalevski et al. 2012) allowing some broad-line visibility even with obscuring matter along our line of sight.

Semi-analytical models (e.g., Venanzi et al. 2020) find that the densest gas sinks closer to the equatorial plane of the AGN, due to asymmetry of the radiation field ($\propto \cos \theta_{\rm axis}$). If the pure geometric unification model applies, this would mean that our

view of the BLR is blocked when looking through angles closer to the equatorial region, whereas at angles higher above the equatorial plane, obscuring matter is distributed more sparsely, and therefore the BLR is more likely to be visible. According to our calculations with the BASS sample, at $-3 < \log \lambda_{\rm Edd} < -2$, the torus rises as high as 56° [calculated using $\theta = 90^{\circ} - \arccos({\rm covering \, factor})$; similarly, torus opening angle = $\arccos({\rm covering \, factor}) = 34^{\circ}$], while the BLR is completely blocked by dense matter up to 37° above the equatorial plane. The geometric unification model, along with these angles and the clumpy structure of the torus, is shown in the top panel of Figure 4.

4.2. High- λ_{Edd} Region: Transitional Timescales

The high- $\lambda_{\rm Edd}$ region gives rise to some seemingly contradictory observational signatures. While overall population studies such as this indicate that the covering factor at high $\lambda_{\rm Edd}$ should be very low if geometric unification applies (e.g., lower panel of Figures 2 and 3 of Ricci et al. (2017b)), observed obscured AGN that are found at these $\lambda_{\rm Edd}$ have very high covering factors. Ricci et al. (2017c) finds that among local ultraluminous infrared galaxies (ULIRGs), the torus covering factor is as high as 95%, and most of these AGN are in late stages of mergers. A recent study of 57 ULIRGs (Yamada et al. 2021) also finds a high covering factor of 66% at $\lambda_{\rm Edd} \simeq 1$. This is quantitatively at odds with a populationaveraged covering factor of <30% at these $\lambda_{\rm Edd}$ (from Figure 2). While ULIRGs represent only a small fraction of the overall AGN population, they dominate infrared samples because they have a lot of dust and they have high covering factors and high $\lambda_{\rm Edd}$. Other obscured high- $\lambda_{\rm Edd}$ populations include red quasars (e.g., Glikman et al. 2004, 2012; Banerji et al. 2015; Glikman et al. 2018), and hot dust-obscured galaxies (HotDOGs, e.g., Assef et al. 2016; Vito et al. 2018). Some X-ray selected studies also find that heavily dustreddened quasars are in a radiatively driven blow-out phase (Lansbury et al. 2020).

In other words, infrared-selected quasars have high covering factors and high $\lambda_{\rm Edd}$. Yet, according to Figure 2, we should find a much smaller obscured/overall ratio, implying a much smaller torus covering factor if simple geometric unification were the cause. As most of these studies conclude that these high- $\lambda_{\rm Edd}$, obscured AGN are in a transitional state, we suggest that the low obscured/overall ratio at high $\lambda_{\rm Edd}$ is indicative of the duration of the obscured phase. That is, the time-averaged covering factor is low ($\sim 30\%$), while infrared studies select luminous/high- $\lambda_{\rm Edd}$ sources that are still in a dust-obscured phase.

To disentangle the geometric and temporal aspects of the evolution of the covering factor, we consider two simple time-dependent parametric models of evolution, described in Section 2.2. In Figure 3, we show these functions constrained using the obscured/overall ratio (from Figure 2) at $\log \lambda_{\rm Edd} = -1.5$ and -1.2, and over the $-1 \leq \log \lambda_{\rm Edd} \leq 0.5$ range. We find that for the first model (sigmoid function), in which the decay of the covering factor might start slowly due to shielding from dense obscuring matter, then accelerate as more matter is removed, the covering factor for the torus approaches zero within 40% of the time spent at $\log \lambda_{\rm Edd} > -1$. The sigmoid function therefore somewhat contradicts infrared studies that find evidence of residual dust around luminous SDSS quasars. The second model (exponential function) accommodates slower

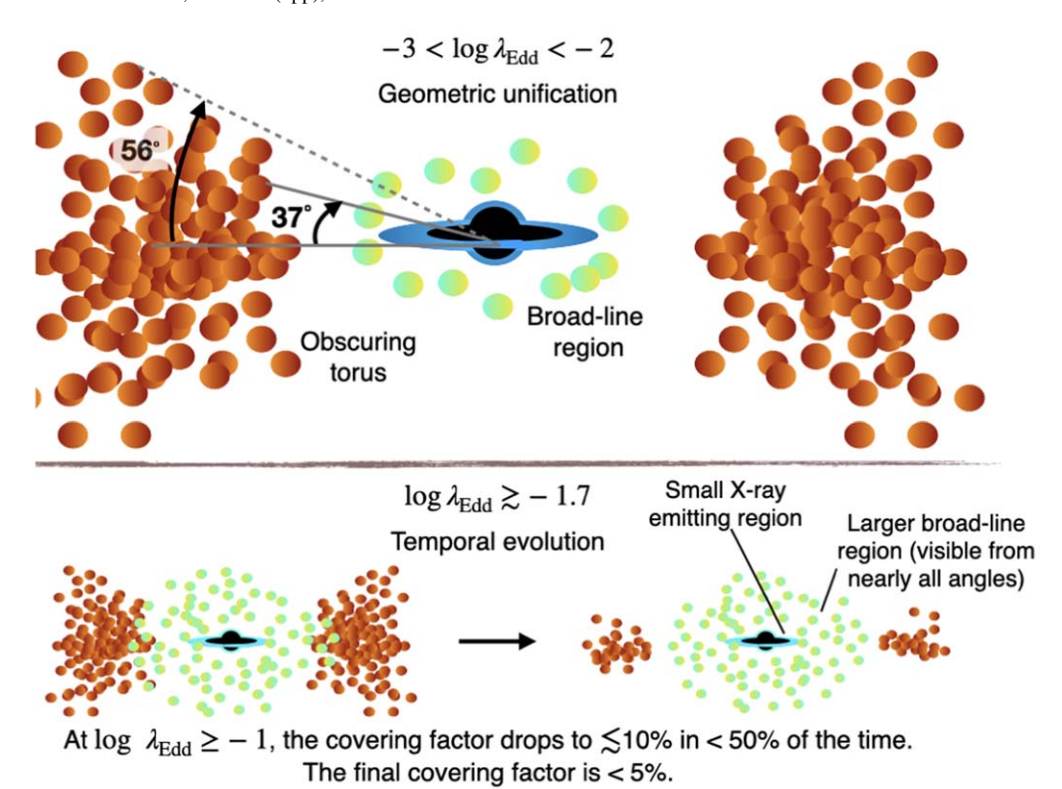


Figure 4. Schematic diagram of AGN circumnuclear structure at low and high Eddington ratios. Top panel: for $\lambda_{Edd} < -2$, radiation pressure is too low to remove dust and gas around the AGN, so the covering factor remains high and differences between obscured and unobscured AGN are likely due to viewing angle. That is, because 80% of AGN have $\log(N_{\rm H}/{\rm cm}^{-2}) > 22$, the torus rises to 56° above the equatorial plane; since optical broad lines' emission are seen in 60% of AGN, the densest gas lies below 37°. Bottom panel: at high $\lambda_{\rm Edd}$, radiation pressure removes the obscuring matter, leaving at most a small persistent covering factor (<5%). We find that BLR is visible from nearly all angles after 30% of the time at this $\lambda_{\rm Edd}$, which may indicate that the height of the BLR region rises above that of the depleted torus

decay of the X-ray detected covering factor, even though the part of the torus that completely blocks BLR is depleted in less than 30% of the AGN lifetime. The *persistent* covering factors, calculated using X-ray obscuration measurements, at $\log \lambda_{\rm Edd} = -1.5$, -1.2, and ~ 0 are $\sim 40\%$, 5%, and 2%, respectively, indicating that at lower $\lambda_{\rm Edd}$, more obscuring matter remains around the AGN at the end of the active phase. The bottom panels of Figure 4 shows a schematic of this transition, with the residual dust (<5% by the end of the phase) in the right panel.

While the exponential function allows a gradual decrease in covering factor, the sigmoid function behaves almost like a step function. If we interpret the sigmoid function as a limiting case where the high- $\lambda_{\rm Edd}$ obscured/total ratio is decided purely by timescale (i.e., an obscured/total ratio of x% means x% of the time is spent fully obscured, and (100-x)% of the time is spent in the almost fully unobscured state), then the percentage of time spent fully obscured by $\log(N_{\rm H}/{\rm cm}^{-2})=22-25$ torus is $24.7^{+4.1}_{-3.4}\%$. The narrow-line only covering factor will be depleted within $10.3^{+5.4}_{-6.7}\%$ of the time, so that for about 15% of the time the AGN will appear broad-line and obscured. This estimate agrees well with the Glikman et al. (2012) and Glikman et al. (2018) results, which suggested that the duration of the red-quasar phase is 15%-20% of the total quasar lifetime.

As both Figures 2 and 3 show, the X-ray measure of obscured/overall ratio at high- $\lambda_{\rm Edd}$ is higher than the type II/overall ratio. A likely interpretation for this is that the former indicates a time-averaged covering factor, while the latter

indicates an increase in the size of the broad-line region relative to the torus. When the scale height of the BLR region is higher than that of the torus, the BLR should be visible even from equatorial lines of sight, as shown in the bottom right panel of Figure 4. This depletion of torus/rise of the BLR happens within 30% of the time spent at $\log \lambda_{\rm Edd} > -1$ (see Figure 3). We do an order-of-magnitude calculation using well-established constraints on the duration of unobscured quasar accretion, which is roughly the Salpeter time of 10^7 – 10^8 yr (Martini 2003; Hopkins et al. 2006; Worseck et al. 2007; Goncalves et al. 2008). Using the functions shown in Figure 3, we estimate that after being triggered to $\log \lambda_{\rm Edd} > -1$, it takes 20%–30% of the time (3–30 Myr) to transition into a completely broad-line phase.

5. Conclusions

This work presents the first *intrinsic* Eddington ratio distribution functions for X-ray-obscured and -unobscured AGN, constrained using the local BASS sample. These ERDFs show that there are \sim 4 times as many obscured as unobscured AGN at low $\lambda_{\rm Edd}$, while the reverse is true at high $\lambda_{\rm Edd}$, with \sim 3 times as many unobscured as obscured AGN.

Reasoning that the circumnuclear obscuration is relatively stable at log $\lambda_{\rm Edd} < -2$, we interpret that population ratio in purely geometric terms. A ratio of 4:1 corresponds to an ${\sim}80\%$ covering factor, meaning that a simple obscuring torus would rise 56° above the equatorial plane. The type II to overall AGN space density ratio, determined by A22, is somewhat smaller, ${\sim}60\%$, with broad optical lines seen in roughly one quarter of

high- $N_{\rm H}$ AGN. This suggests that the obscuring torus is clumpy. Recent simulations suggest that obscuration is densest near the equatorial plane (e.g., Venanzi et al. 2020). In that case, all broad lines are blocked within 37° of the plane by tightly packed obscuring matter, with some open lines of sight between 37° and 56°. The top panel of Figure 4 shows a schematic representation of this clumpy torus, with geometry derived from the ERDF ratios.

At high Eddington ratios, the fraction of obscured AGN is much smaller. Additionally, the obscured fraction is much lower for narrow-line AGN (\sim 5%) than for AGN with $\log(N_{\rm H}/{\rm cm}^{-2}) > 22$ (\sim 30%; see bottom panel of Figure 2). Infrared-selected luminous, high- $\lambda_{\rm Edd}$, obscured AGN have very high covering factors (66%–95%; see Section 4.2), much higher than the observed population average. This tension can be resolved if the highly covered phase is short-lived and infrared-luminous, so that infrared selection preferentially finds ULIRGs, red quasars, and HotDOGs.

To disentangle the geometric and temporal aspects at high $\lambda_{\rm Edd}$, we considered two simple physically motivated models of the decline in covering factor with time (Figure 3), constrained by the obscured/overall ratios at high $\lambda_{\rm Edd}$. Using these models, we find that it takes approximately 50% of the lifetime of the high- $\lambda_{\rm Edd}$ phase (i.e., at $\log \lambda_{\rm Edd} > -1$) to reduce the covering factor from 80% to $\sim 10\%$. The covering factor is <5% at the end of the high- $\lambda_{\rm Edd}$ phase. Additionally, the broad-line region becomes visible along all lines of sight within 20%–30% of the time (orange and yellow lines in Figure 3), possibly indicating that the height of the broad-line region is higher than that of the obscuring torus, making it visible along all lines of sight, as shown in the bottom right panel of Figure 4.

We thank the referee for the thoughtful comments that helped us greatly improve this Letter. This Letter is part of a series presented by the BASS Collaboration. Specifically, this is BASS XXXVIII. T.T.A. acknowledges support from NASA through ADAP award NNH22ZDA001N. T.T.A. and R.C.H. acknowledge support from NASA through ADAP award 80NSSC19K0580, and the National Science Foundation through CAREER award 1554584. C.M.U. acknowledges support from the National Science Foundation under grant No. AST-1715512, and from NASA through ADAP award 80NSSC18K0418. P.N. acknowledges the black hole Initiative (BHI) at Harvard University, which is supported by grants from the Gordon and Betty Moore Foundation and the John Templeton Foundation. B.T. acknowledges support from the Israel Science Foundation (grant No. 1849/19) and from the European Research Council (ERC) under the European Union's Horizon 2020 research and innovation program (grant agreement No. 950533). M.K. acknowledges support from NASA through ADAP award NNH16CT03C. M.B. acknowledges support from the YCAA Prize Postdoctoral Fellowship. K.O. acknowledges the support of the Korea Astronomy and Space Science Institute under the R&D program (Project No. 2022-1-830-06) supervised by the Ministry of Science and ICT and from the National Research Foundation of Korea (NRF-2020R1C1C1005462). We acknowledge funding support through ANID programs: Millennium Science Initiative NCN19_058 (E.T.), ICN12_009 (FEB); CATA-BASAL -ACE210002 (E.T., F.E.B.), and FB210003 (E.T., F.E.B., C.R.); FONDECYT Regular - 1190818 (E.T., F.E.B.) and 1200495

(F.E.B., E.T.); and FONDECYT Iniciacion 11190831 (C.R.). This work was performed in part at the Aspen Center for Physics, which is supported by National Science Foundation grant PHY-1607611.

ORCID iDs

Tonima Tasnim Ananna https://orcid.org/0000-0001-8211-3807 C. Megan Urry https://orcid.org/0000-0002-0745-9792 Claudio Ricci https://orcid.org/0000-0001-5231-2645 Priyamvada Natarajan https://orcid.org/0000-0002-5554-8896 Ryan C. Hickox https://orcid.org/0000-0003-1468-9526 Benny Trakhtenbrot https://orcid.org/0000-0002-3683-7297 Ezequiel Treister https://orcid.org/0000-0001-7568-6412 Anna K. Weigel https://orcid.org/0000-0002-5489-4316 Yoshihiro Ueda https://orcid.org/0000-0001-7821-6715 Michael J. Koss https://orcid.org/0000-0002-7998-9581 F. E. Bauer https://orcid.org/0000-0002-8686-8737 Matthew J. Temple https://orcid.org/0000-0001-8433-550X Mislav Baloković https://orcid.org/0000-0003-0476-6647 Richard Mushotzky https://orcid.org/0000-0002-7962-5446 Connor Auge https://orcid.org/0000-0002-5504-8752 David B. Sanders https://orcid.org/0000-0002-1233-9998 Darshan Kakkad https://orcid.org/0000-0002-2603-2639 Lia F. Sartori https://orcid.org/0000-0001-8020-3884 Stefano Marchesi https://orcid.org/0000-0001-5544-0749 Daniel Stern https://orcid.org/0000-0003-2686-9241 Kyuseok Oh https://orcid.org/0000-0002-5037-951X Turgay Caglar https://orcid.org/0000-0002-9144-2255 Meredith C. Powell https://orcid.org/0000-0003-2284-8603 Stephanie A. Podjed https://orcid.org/0000-0002-0504-565X Julian E. Mejía-Restrepo https://orcid.org/0000-0001-8450-7463

References

Ananna, T. T., Treister, E., Urry, C.M., et al. 2019, ApJ, 871, 240 Ananna, T. T., Weigel, A. K., Trakhtenbrot, B., et al. 2022, ApJS, 261, 9 Antonucci, R. 1993, ARA&A, 31, 473 Assef, R. J., Walton, D. J., Brightman, M., et al. 2016, ApJ, 819, 111 Banerji, M., Alaghband-Zadeh, S., Hewett, P. C., & McMahon, R. G. 2015, MNRAS, 447, 3368 Barger, A. J., Cowie, L. L., Mushotzky, R. F., et al. 2005, AJ, 129, 578 Baumgartner, W. H., Tueller, J., Markwardt, C. B., et al. 2013, ApJS, 207, 19 Best, P. N., Kauffmann, G., Heckman, T. M., et al. 2005, MNRAS, 362, 25 Braito, V., Reeves, J. N., Gofford, J., et al. 2014, ApJ, 795, 87 Elitzur, M. 2012, ApJ, 747, L33 Fabian, A. C., Celotti, A., & Erlund, M. C. 2006, MNRAS, 373, L16 Fabian, A. C., Vasudevan, R. V., & Gandhi, P. 2008, MNRAS, 385, L43 Foreman-Mackey, D., Hogg, D. W., Lang, D., & Goodman, J. 2013, PASP, Gilli, R., Comastri, A., & Hasinger, G. 2007, A&A, 463, 79 Glikman, E., Gregg, M. D., Lacy, M., et al. 2004, ApJ, 607, 60 Glikman, E., Lacy, M., LaMassa, S., et al. 2018, ApJ, 861, 37 Glikman, E., Urrutia, T., Lacy, M., et al. 2012, ApJ, 757, 51 Goncalves, T. S., Steidel, C. C., & Pettini, M. 2008, ApJ, 676, 816 Green, P. J., Pulgarin-Duque, L., Anderson, S. F., et al. 2022, ApJ, 933, Hall, P., Hopkins, P., Strauss, M., Richards, G., & Brinkmann, J. 2004, in ASP Conf. Ser., 311, AGN Physics with the Sloan Digital Sky Survey, ed. G. T. Richards & P. B. Hall (San Francisco, CA: ASP), 65 Hopkins, P. F., Somerville, R. S., Hernquist, L., et al. 2006, ApJ, 652, 864

Hopkins, P. F., Strauss, M. A., Hall, P. B., et al. 2004, AJ, 128, 1112

Kelly, B. C., & Shen, Y. 2013, ApJ, 764, 45

```
Koss, M. J., Assef, R., Balokovic, M., et al. 2016, ApJ, 825, 85
Koss, M. J., Ricci, C., Trakhtenbrot, B., et al. 2022a, ApJS, 261, 2
Koss, M. J., Trakhtenbrot, B., Ricci, C., et al. 2022b, ApJS, 261, 1
Koss, M. J., Trakhtenbrot, B., Ricci, C., et al. 2022c, ApJS, 261, 6
La Franca, F., Fiore, F., Comastri, A., et al. 2005, ApJ, 635, 864
Lansbury, G. B., Banerji, M., Fabian, A. C., & Temple, M. J. 2020, MNRAS,
   495, 2652
Lawrence, A. 1991, MNRAS, 252, 586
Marchese, E., Braito, V., Della Ceca, R., Caccianiga, A., & Severgnini, P.
  2012, MNRAS, 421, 1803
Martini, P. 2003, in Coevolution of Black Holes and Galaxies, ed. L. C. Ho
   (Cambridge: Cambridge Univ. Press), 169
Mejia-Restrepo, J. E., Trakhtenbrot, B., Koss, M. J., et al. 2022, ApJS, 261, 5
Netzer, H. 2015, ARA&A, 53, 365
Oh, K., Yi, S. K., Schawinski, K., et al. 2015, ApJS, 219, 1
Ramos Almeida, C., Levenson, N. A., Rodriguez Espinosa, J. M., et al. 2009,
   ApJ, 702, 1127
Ricci, C., Ananna, T. T., Temple, M. J., et al. 2022, ApJ, 938, 67
Ricci, C., Bauer, F. E., Treister, E., et al. 2017c, MNRAS, 468, 1273
```

Ricci, C., Trakhtenbrot, B., Koss, M. J., et al. 2017a, ApJS, 233, 17

```
Ricci, C., Trakhtenbrot, B., Koss, M. J., et al. 2017b, Natur, 549, 488
Ricci, C., Ueda, Y., Koss, M. J., et al. 2015, ApJL, 815, L13
Richards, G. T., Fan, X., Newberg, H. J., et al. 2002, AJ, 123, 2945
Schulze, A., Bongiorno, A., Gavignaud, I., et al. 2015, MNRAS, 447, 2085
Simpson, C. 2005, MNRAS, 360, 565
Stalevski, M., Fritz, J., Baes, M., Nakos, T., & Popović, L. Č. 2012, MNRAS,
  420, 2756
Stawarz, L. 2010, in ASP Conference Series, Vol. 427, Accretion and Ejection
  in AGN: a Global View, ed. L. Maraschi (San Francisco, CA: ASP), 357
Trakhtenbrot, B., Arcavi, I., MacLeod, C. L., et al. 2019, ApJ, 883, 94
Treister, E., Krolik, J. H., & Dullemond, C. 2008, ApJ, 679, 140
Treister, E., Urry, C. M., Chatzichristou, E., et al. 2004, ApJ, 616, 123
Treister, E., Urry, C. M., & Virani, S. 2009, ApJ, 696, 110
Ueda, Y., Akiyama, M., Ohta, K., & Miyaji, T. 2003, ApJ, 598, 886
Urry, C. M., & Padovani, P. 1995, PASP, 107, 803
Venanzi, M., Honig, S., & Williamson, D. 2020, ApJ, 900, 174
Vito, F., Brandt, W. N., Stern, D., et al. 2018, MNRAS, 474, 4528
Worseck, G., Fechner, C., Wisotzki, L., & Dall'Aglio, A. 2007, A&A,
  473, 805
Yamada, S., Ueda, Y., Tanimoto, A., et al. 2021, ApJS, 257, 61
```